OPTICA

Breakdown of the single-collision condition for soft x-ray high harmonic generation in noble gases

Pierre-Alexis Chevreuil,[1,*] Fabian Brunner,[1] Uwe Thumm,[2] Ursula Keller,[1] and Lukas Gallmann[1]

[1]ETH Zurich, Department of Physics, Institute for Quantum Electronics, Auguste-Piccard-Hof 1, 8093 Zurich, Switzerland
[2]Department of Physics, Kansas State University, Manhattan, Kansas 66506, USA
*Corresponding author: pierre-alexis.chevreuil@laposte.net

Received 9 August 2022; revised 28 October 2022; accepted 31 October 2022; published 20 December 2022

High harmonic generation (HHG) in atomic gases is generally assumed to originate from photoelectrons that are not perturbed by neighboring particles. In this paper, we study theoretically and experimentally the regime where this approximation breaks down. At high laser intensities, we experimentally find that producing soft x-rays beyond this single-collision condition leads to a strong reduction of the coherent HHG response and appearance of incoherent radiation. We generalize our results to phase-matched HHG with mid-infrared drivers, and determine that a *minimum pulse energy* is needed to simultaneously phase match the HHG process and keep photoelectrons unperturbed by surrounding particles. Therefore, while previous research showed that HHG efficiency is independent of the driving pulse energy if other experimental parameters are scaled accordingly, we find that this rule no longer applies for high photon energies. Our study thus provides important guidelines for the laser parameters needed for the generation of high flux soft x-ray high harmonics.

https://doi.org/10.1364/OPTICA.471084

1. INTRODUCTION

High harmonic generation (HHG) is an extremely nonlinear process that converts intense laser radiation into extreme ultraviolet (XUV) or soft x-ray (SXR) radiation. While a macroscopic build-up (phase matching) of the SXR radiation is necessary to obtain a significant HHG flux, the light generation in gaseous targets can be explained at the level of a single atom through the so-called three-step model [1,2]. In this framework, it is assumed at the microscopic level that the ion and its liberated electron are isolated from other atoms, ions, and electrons in the gas, and in particular that the ejected electron does not collide with neighboring particles during its propagation in the continuum. In the following, we will refer to this as the single-collision condition (SCC). We show in Fig. 1 a sketch describing a scenario where the SCC is met, and another one where it is not.

For photon energies below 100 eV, the electron excursion in the continuum is typically of the order of a few nm and the phase-matching pressures are generally on the order of a few mbar to a bar. This corresponds to interatomic distances of the order of a few tens of nm up to several μm, which implies that the SCC holds. By contrast, generating higher photon energies requires the electron to gain more kinetic energy before recombination. In most cases, this translates into longer electron excursion distances. In addition, photon energies above 0.3 keV are usually generated using a short- or mid-wavelength infrared driver, where phase-matching pressures are generally of the order of a few bar to several tens of bar [3–6] because of the refractive index of the gas approaching unity. Those two facts combined imply that beyond a certain photon energy, most photoelectrons producing high harmonics will interact with surrounding particles during their propagation in the continuum, such that the SCC does not hold anymore. In this paper, we study theoretically and experimentally the transition regime where the SCC breaks down and give simple guidelines on how to overcome this limitation.

2. THEORY

One of the most accurate ways of describing the effect of surrounding atoms on the HHG spectrum is to solve the three-dimensional time-dependent Schrödinger equation with the combined potentials of many atoms. Such work has already been performed [7], but only for a limited set of parameters. To obtain more general results applicable to different pressures, wavelengths, and intensities, we propose a simple analytical model to obtain estimates for when the SCC is valid or not, and test it with our experimental results. For this, we compare two parameters: the electron excursion in the continuum before collision with its parent ion and the average distance a free electron can travel before colliding with another atom.

To obtain the simplest model possible, we neglect electron–electron and electron–ion interactions and consider only interactions of the electron with neutral atoms. This is well justified for phase-matched SXR HHG since the ionization level is relatively low [8].

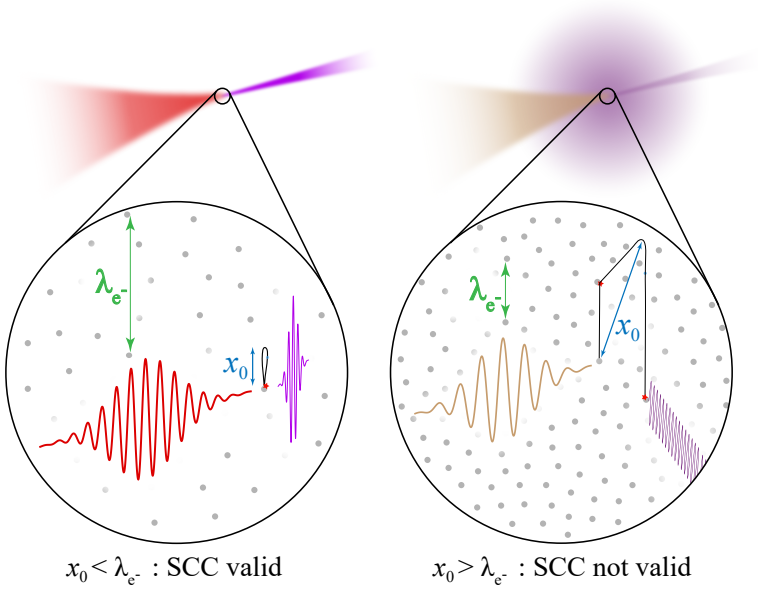

Fig. 1. Sketch depicting the single-collision condition (SCC). When the electron excursion in the continuum x_0 is smaller than the electron mean free path λ_{e^-} (as in most XUV-HHG sources), the electron is normally unperturbed by surrounding particles during its excursion in the continuum. In the case where $x_0 > \lambda_{e^-}$ (as in some SXR-HHG cases), the electron is likely to be scattered by a surrounding particle, leading to a decrease of the coherent HHG response and an increase of the spatially and temporally incoherent radiation.

A. Electron Mean Free Path

In the kinetic theory of gases, each particle has a non-zero velocity due to thermal motion, leading to random collisions between gas particles. The average distance a particle can travel before colliding with another one is referred to as the mean free path, and the sphere in which a scattering event is likely to happen is described by the so-called kinetic diameter [9]. In our case, we study atom–electron collisions instead of atom–atom collisions. We therefore need to know the average distance traveled by a photoelectron before collision with another atom. We refer to this distance as the electron mean free path λ_{e^-}.

To estimate this quantity, instead of considering the collision between two atoms modeled by hard spheres (HS) with the same kinetic diameter, we replace one of the collision bodies by an electron, which we assume to have zero kinetic diameter. As justified in Supplement 1, due to the large electric fields needed to generate high harmonics, we can make the simplification $k_B T \ll E_{\mathrm{kin},e^-}$. We then find that the electron mean free path is (details about the calculation are given in Supplement 1)

$$\lambda_{e^-} = \frac{4 k_B T}{\pi p d^2}, \tag{1}$$

where λ_{e^-} is the electron mean free path, k_B the Boltzmann constant, T the gas temperature, and d the kinetic diameter of the atom [9]. In Fig. 2, we show how the electron mean free path scales with gas pressure p for all gases studied in this paper.

B. Analytical Estimates of the Peak Intensities Needed for SCC Breakdown

We now compute the electron excursion in the continuum. In phase-matched SXR-HHG experiments, ground-state depletion is generally low [8]; we can therefore neglect it here. The maximum electron excursion for an electron producing HHG from a linearly

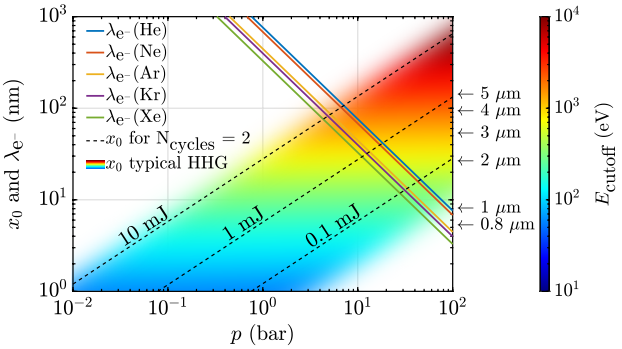

Fig. 2. Colored solid lines represent the electron mean free path λ_{e^-} for different gases calculated at $T = 293$ K using Eq. (1) and using the kinetic diameters from [10]. The dashed iso-lines show the maximum electron excursion x_0 for phase-matched cutoff harmonics for two-cycle pulses in He with different pulse energies, and the color-shaded area represents the corresponding cutoff energies for pulse energies between 0.1 and 10 mJ and pulse durations between two and six cycles. In all cases, the wavelength and peak intensities are adjusted to remain below the critical ionization level [11]. Details on the calculation are given in Supplement 1.

polarized laser field is then given by (details about the calculation are given in Supplement 1)

$$x_0 = \frac{q_e \sqrt{2 Z_0 I_{\mathrm{peak}}} \lambda_{\mathrm{laser}}^2}{2\pi^2 c^2 m_e}, \tag{2}$$

where q_e is the elementary charge, Z_0 the vacuum impedance, I_{peak} the laser peak intensity, λ_{laser} the laser wavelength, c the speed of light, and m_e the electron mass.

As shown in Supplement 1, it is possible from the laser wavelength and the driving field pulse duration to compute the maximum cutoff energy that can be phase matched and the peak intensity of the driving field at which those harmonics are produced. Since no simple exact relationship between all

Table 1. Estimated Intensities above which the SCC Is Expected to Break Down for Our Experimental Parameters

Gas	I_{SCC} $(W \cdot cm^{-2})^a$	$d(Å)^b$	$\epsilon/k_B\ (K)^c$
He	4×10^{17}	2.556	10.22
Ne	3×10^{17}	2.749	35.60
Ar	1×10^{17}	3.405	119.8
Kr	1×10^{17}	3.597	158
Xe	7×10^{16}	3.963	217

[a]The I_SCC values are computed using Eq. (3).
[b]Values of d and ϵ/k_B come from Ref. [10].
[c]ϵ/k_B is the minimum of the Lennard-Jones (LN) potential, which will be used in Section 4.B [10].

those quantities can be derived, we show in Fig. 2 the maximum collision-free electron excursion for phase-matched HHG in He for typical experimental parameters. For the pressures used in most XUV-HHG experiments, Fig. 2 shows that the SCC holds. However, as one aims to increase the cutoff energy, the maximum electron excursion x_0 becomes comparable to the electron mean free path λ_{e^-}, such that the SCC is not fulfilled anymore.

To generate high photon energies, high laser intensities or long wavelengths can be used, since the HHG cutoff scales as $E_{cutoff} = I_p + 3.17U_p$, where I_p represents the ionization potential of the gas, and $U_p \propto I_{laser} \cdot \lambda_{laser}^2$ [12]. In this section, we will focus on the intensity-scaling approach, as it is the approach we could study in detail experimentally, and in Section 4, we will also consider the wavelength-scaling approach. From Eqs. (1) and (2), we can then estimate the intensity at which $x_0 = \lambda_{e^-}$, which determines the limiting intensity for the validity of the SCC:

$$I_{SCC} = \frac{1}{2Z_0}\left(\frac{8\pi k_B m_e c^2}{q_e}\frac{T}{d^2 p \lambda_{laser}^2}\right)^2. \quad (3)$$

In our experiment, the gas is sent through an open-ended nozzle at a pressure of ∼10 bar before undergoing a supersonic expansion into vacuum. We therefore estimate $p \approx 5$ bar and $T \approx 200$ K in the interaction region for our non-phase-matched experiment [13]. With those parameters, we find SCC intensities of the order of 10^{17} W · cm^{-2} for all noble gases, as shown in Table 1. Experimentally, we observe that the SCC breaks down already at intensities approximately four times lower than those predicted by Eq. (3), as we will see in Section 3.

C. Simulation

The predicted SCC intensities are all well within the barrier suppression ionization (BSI) regime [14] for all noble gases, implying that the electron release times—and by extension x_0—differ significantly from a tunneling scenario, and that ground-state depletion cannot be neglected.

To find more accurate estimates for electron excursions for our experimental conditions, we use a three-dimensional classical trajectory Monte Carlo (CTMC) simulation that includes a time-dependent Coulomb field and that accounts for the magnetic component of the Lorentz force. More details about the simulation can be found in Supplement 1.

First, we will study trajectories that recombine with their parent ion, namely, that produce high harmonics. For this, we consider all trajectories that enter a recombination sphere of 5 a.u. around the parent ion as producing harmonics [15] and record their maximum excursion during the first optical cycle following ionization. In Fig. 3(a), we compare the simulation results with the predictions from Eq. (2). The excursion range of electrons generating harmonics is smaller than the analytical model prediction mostly because of ground-state depletion and the initial momentum of the photoelectron at the moment of ionization in the case of BSI [16].

However, not all electrons recombine with their parent ion. For those remaining electrons, the simulation indicates that their average excursion within one cycle after ionization is up to three times higher than for recombining electrons. Interaction with a surrounding particle can then lead to the emission of light or a modification of the electron kinetic energy, or both. We therefore examine in Fig. 3(b) the kinetic energy of those non-recombining electrons at the end of the laser pulse.

For linear polarization, the spectrum has a clear maximum at zero kinetic energy for all noble gases, mostly because the momentum gained by the electron during one half cycle is almost fully canceled out during the next half cycle. Indeed, under the slowly varying envelope approximation, the amplitude of the electric field at a given time and one cycle later is almost the same, leading to a relatively small net energy gain at the end of the pulse.

For circular polarization, the peak of the electric field is $\sqrt{2}$ smaller than for the linear polarization case at the same peak intensity. Moreover, the circularly polarized field mostly pushes the electron away from the ion without ever bringing it back to its parent ion. Overall, this leads to the emission of a higher number of high energy electrons as compared to the linear polarization case [Fig. 3(b)]. It is important to note, however, that the highest

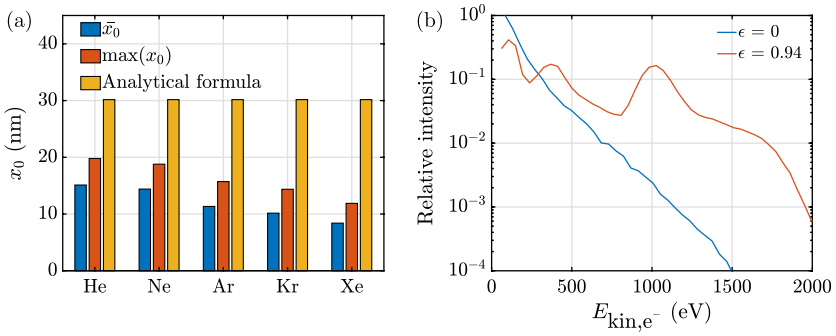

Fig. 3. CTMC simulation results for a 10 fs pulse centered at 0.8 μm with a peak intensity of 3×10^{16} W · cm^{-2}. (a) Average and maximum electron excursion in a linearly polarized field during the first laser cycle after ionization for electrons producing harmonics, compared with Eq. (2). (b) Electron kinetic energy E_{kin,e^-} spectrum for non-recolliding electrons in Ar at the end of the pulse for linear polarization ($\epsilon = 0$) and close-to-circular polarization ($\epsilon = 0.94$).

electron kinetic energies are still reached with linear polarization, since the peak of the electric field is higher.

D. SXR Generation at High Intensities beyond the SCC Breakdown

As Fig. 3(a) shows, Eq. (2) correctly estimates the order of magnitude of the electron excursion, even for very high laser intensities. Thus, we can now consider the effects expected from generating SXR beyond the SCC, which corresponds to $x_0 > \lambda_{e^-}$. As a first effect, we expect a perturbation of the microscopic HHG response. Indeed, an earlier simulation showed that at intensities of $\sim 10^{14}$ W · cm^{-2}, the phase acquired by the electron wave packet in the continuum starts to be modified by surrounding particles for ionic densities between 10^{18} and 10^{20} cm^{-3} [7]. This modification primarily impacts the long trajectories, leading to a narrowing of the harmonic lines and a shortening of the XUV pulse duration.

On top of the modification of the HHG spectrum, one can also expect a decrease of the microscopic HHG response, because the scattering of the electron wave packet by surrounding atoms can cause it to miss its parent ion.

Another effect to be expected is a direct recombination of the photoelectrons with neighboring ions without previous scattering by other particles. It was numerically predicted [17] that such recombination would lead to the appearance of an extended HHG cutoff, beyond the usual $I_p + 3.17U_p$, with isotropically emitted SXR light, as Fig. 1(b) illustrates. The order of magnitude of the SXR pulse duration would, however, remain the same as the duration of the driver.

Finally, if the ionic density is high enough, it is possible that collisional plasma excitation through inverse bremsstrahlung starts to play a role in the ionization dynamics. Ditmire *et al.* showed that for a 0.8 μm, 100 fs pulse focused to 10^{16} W · cm^{-2}, inverse collisional bremsstrahlung becomes the dominant ionization process when the ion density is above $\sim 10^{19}$ cm^{-3} [18]. In that case, the light emission happens mostly through the thermal cool-down of the plasma, leading to a SXR pulse duration given by the thermalization time of the plasma, which is typically on the ns time scale.

3. EXPERIMENT

A. Experimental Setup

In our experiment, we use a 0.8 μm optical parametric chirped pulse amplifier (OPCPA) delivering 10 fs pulses with up to 34 W of average power after compression at 100 kHz repetition rate [19]. For SXR generation, we use the same setup for generation and detection as in [20], and we thus focus the beam to an estimated intensity of 3×10^{16} W · cm^{-2} on noble gases supplied at ∼10 bar. The gas is provided through an open-ended nozzle with 0.2 mm inner diameter.

In our previous investigation [20], we found that using a drilled gas cell filled with He or Ne leads to approximately the same SXR flux as with an open-ended nozzle. However, when we replace He or Ne by Ar, Kr, or Xe, we do not observe any light between 0.1 and 1 keV photon energy, likely because of the larger B integral and plasma defocusing, which can both decrease the peak intensity in the high pressure zone. In this study, we therefore use only an open-ended nozzle where such effects are minimized.

B. Experimental Results

As discussed above, in this regime of intensities and pressures, both coherent and incoherent SXR emissions are possible. To assess the coherence of the radiation, we vary the polarization from linear to circular by placing an achromatic quarter-wave plate (λ/4; RAC 5.4, Bernhard Halle Nachfl. GmbH) in the beam. The strong dependence of the HHG efficiency on ellipticity [2] should then allow us to discern HHG from incoherent emission. The ellipticity calibration procedure is provided in Supplement 1.

In the left column of Fig. 4, we show the SXR spectra obtained in He, Ne, Ar, Kr, and Xe. We observe in He, Ne, Kr, and Xe that the SXR flux decreases for increasing ellipticity in some photon energy ranges, which can be due to either the presence of HHG or the incoherent radiation generated by the higher kinetic energy electrons that are freed with linear polarization, as discussed above. To distinguish between these two possibilities, we perform a second experiment where we observe the SXR light perpendicular to the laser propagation direction, since HHG is known to be emitted in a spatially confined beam along the driver pulse propagation direction, while incoherent radiation is emitted isotropically. We also change the polarization state with the same λ/4 to find whether the SXR we observe originates from thermal plasma cool-down or inner-shell excitation from direct recollision [21–23]. We show in the right column of Fig. 4 the SXR spectra obtained perpendicular to the laser propagation direction with illumination conditions remaining as close as possible to the first experiment.

C. Discussion of the Experimental Results in He and Ne

Comparing the left and right columns allows for an unambiguous identification of HHG and incoherent radiation within the small variations of experimental parameters. It is clear that both in He and Ne, HHG is present between 200 and 600 eV. However, while we do not observe any SXR light from He when measuring at 90° with respect to the laser propagation direction with linear polarization, we observe a small background in Ne, showing the simultaneous presence of HHG and incoherent plasma radiation at the same photon energies.

Although the level of incoherent radiation remains low compared to the coherent beam within the solid angle seen by the spectrometer, it demonstrates the importance of verifying the coherence of the beam, in particular for HHG driven at high intensity [24]. We note that this verification cannot be made by observing only the spectrally integrated HHG beam, since both coherent and incoherent radiation can co-exist at the same photon energies.

In He, we observe incoherent radiation only when the polarization is close to circular. This is in good agreement with our CTMC simulation, which predicts the generation of a relatively large number of high energy electrons for circular polarization. Interestingly, in Ne, we observe a weak line around 800–850 eV, which is close to the ionization potential of a Ne K-shell electron. This may originate from laser-accelerated valence electrons reaching sufficiently high energies to excite core electrons to the valence levels. Recombination may then lead to SXR emission [21–23]. However, contrary to [21–23], we do not observe a dipole-like emission pattern when rotating the polarization plane. We assign this to an emission originating mostly from indirect recollisions, as suggested in [23].

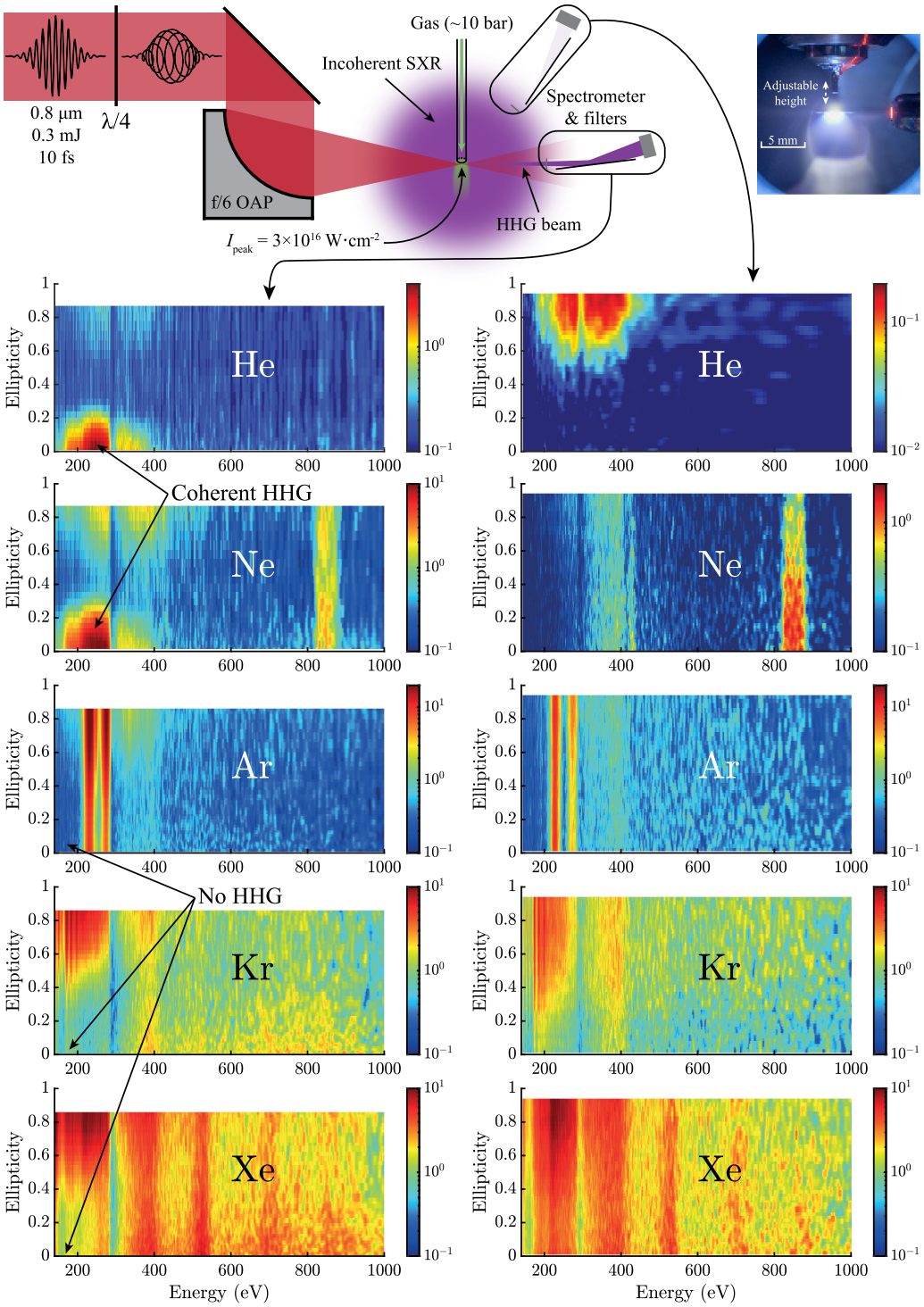

Fig. 4. Experimental SXR spectra showing the transition between SXR originating mostly from HHG in light gases (He, Ne) to SXR generation dominated by incoherent radiation when using heavier gases (Ar, Kr, Xe). The left and right columns show the SXR yield measured along and perpendicular to the laser propagation direction, respectively. The distance between the nozzle and the focus is ∼30 μm. The spectra are not corrected for the transmission characteristics of the filters, CCD efficiency, and grating reflectivity to improve readability. The features around 280 and 400 eV originate from organic deposits in the beamline and the Ag filter, respectively. All color bars on the sides of the graphs have units of counts · pixel^{-1} · s^{-1}. In He and Ne, the graphs on the left and right columns have different color scales because the HHG flux is much higher than the incoherent radiation. OAP, off-axis parabola.

D. Discussion of the Experimental Results in Ar, Kr, and Xe

Surprisingly, most of the SXR emission from Ar is spatially incoherent, demonstrating that the microscopic HHG response is almost completely suppressed by interactions with surrounding atoms, and that the SCC is not met. Since we observed some coherent radiation in Ne but not in Ar, it is interesting to determine the ratio x_0/λ_{e^-} in both gases. For our experimental parameters at the interaction point (∼5 bar, 200 K for all gases), and using the

results from the CTMC simulations for x_0, we find $x_0/\lambda_{e^-} \approx 0.20$ in Ne and $x_0/\lambda_{e^-} \approx 0.26$ in Ar.

Despite the modest difference of x_0/λ_{e^-} in both cases, the transition between the HHG-dominated and incoherent-dominated regimes is relatively sharp between the two gases. This may be due to the large difference of the electron mean free path of Ne and Ar at electron kinetic energies between 0.1 and 1 keV, as shown in Supplement 1. Since the spectrometer entrance slit (7×1 mm^2) is located 0.8 m from the generation point, this implies that the spatially integrated incoherent SXR flux is at least 10^6 times more intense than the co-propagating coherent HHG beam.

When switching from Ar to Kr, we observe a substantial SXR flux increase, consistent with the lower ionization potential of Kr, leading to the release of more electrons, which heats the plasma more efficiently. As in Ar, most of the emission is incoherent. As for the other gases, the SXR flux greatly increases when the polarization is close to circular, due to the larger number of high energy electrons being released compared to the linear polarization case. Finally, we find that the flux in Xe is even higher than for Kr. We attribute this to the even lower ionization potential of Xe.

Yet, it is worth noting that the x-ray flux generated in Kr and Xe between 0.6 and 1 keV is significantly higher along the beam propagation direction compared to perpendicular to it. Moreover, for Kr and Xe, the x-ray yield along the beam propagation direction decreases with increasing ellipticity in this photon energy range. These two observations are consistent with the presence of HHG. Interestingly, a recent study where laser pulses with a peak intensity of 2.5×10^{16} W $\cdot$ cm^{-2} were focused into 0.9 bar of Kr also seems to indicate that coherent radiation between at least 2 and 5 keV can originate from highly multivalent ions [25].

While further research is required to explain the extreme beam divergence of the claimed harmonic emission and to determine the ratio of coherent light over incoherent light, SXR emission from multiply charged ions may also at least partially explain our observations in Kr and Xe between 0.6 and 1 keV. Assuming a coherent origin of the SXR light in our experiment, which uses few-cycle pulses, the harmonic flux may have been increased by the non-adiabatic self-phase-matching (NSPM) process, which manifests itself mostly at high photon energies [24,26–28]. In that case, one possible reason that harmonics would be present at high photon energies and not at low photon energies would be due to the lower interaction of high kinetic energy electrons with surrounding particles compared to electrons with lower kinetic energy. A second possible explanation is that the strong plasma-induced defocusing leads the long electron trajectories to contribute more strongly to the coherent flux than short trajectories [29].

4. GENERALIZATION AND IMPLICATIONS FOR PHASE-MATCHED SXR HHG

A. Pressure Required for Phase Matching

SXR-HHG photons can be generated by using high laser intensities or by using a long-wavelength driver [20]. Since the previous section showed that the high intensity approach leads to a reduction of the coherent response accompanied by an increase of the incoherent radiation when $x_0 \gtrsim 0.2\lambda_{e^-}$ for our experimental parameters, we will now study the second approach to generate SXR high harmonics, which consists of using a long-wavelength driver in a phase-matched regime with intensities typically of the order of a few 10^{14} W $\cdot$ cm^{-2}.

Phase matching the HHG process is achieved by matching the phase velocities of the infrared and generated SXR waves, which is attained by balancing the neutral dispersion, dipole, plasma dispersion, self-phase modulation, and Gouy phase-mismatch factors [4]. Experimentally, this is often done by tuning the pressure and maximizing the HHG flux. At the focus, the dipole phase mismatch vanishes, and phase matching is obtained when the neutral dispersion phase-mismatch factor compensates for the plasma dispersion, Gouy phase, and self-phase modulation phase-mismatch contributions. At the focus, the phase-matching pressure then reads [30]

$$p(\Delta k = 0) = p_0 \frac{I_{\text{peak}} \lambda_{\text{laser}}^3 N_{\text{cycles}}}{2\pi c K_1 K_2 E_{\text{pulse}} \Delta n \left(1 - \frac{\eta}{\eta_c}\right)}, \tag{4}$$

where p_0 is the standard pressure (10^5 Pa), and N_{cycles} is the number of optical cycles of the laser pulse. K_1 and K_2 are correction factors for the peak fluence and peak intensity of the laser pulse compared to their equivalents for a square-shaped pulse (2.0 and 0.94 for a spatially and temporally Gaussian beam, respectively). E_{pulse} is the pulse energy, Δn the difference of the refractive index of the gas between the fundamental laser wavelength and the cutoff wavelength at ambient temperature and pressure, η the ionization level at the peak of the pulse, and η_c the critical ionization level [30]. Equation (4) indicates that phase matching is possible only if $\eta < \eta_c$, which sets an upper limit on the laser intensity that can be used to produce phase-matched high harmonics.

B. Minimum Pulse Energy Required to Generate Phase-Matched Harmonics within the SCC

Combining Eqs. (1) and (4), we find that the electron mean free path at the phase-matching pressure scales as $\lambda_{e^-}^{\Delta k=0} \propto I_{\text{peak}}^{-1} \lambda_{\text{laser}}^{-3}$. At the same time, the critical ionization level for phase-matched SXR HHG is of the order of a percent or below; Eq. (2) is then an excellent approximation for x_0 and shows that the electron excursion scales as $x_0 \propto \sqrt{I_{\text{peak}}} \lambda_{\text{laser}}^2$. Because of how the peak intensity needed to reach the critical ionization level scales with wavelength, we find that $x_0 > \lambda_{e^-}$ if the pressure is higher than

$$p(x_0 = \lambda_{e^-}) = \frac{8\pi m_e c^2 k_B T}{d^2 q_e \sqrt{2 Z_0 I_{\text{peak}}} \lambda_{\text{laser}}^2}. \tag{5}$$

Therefore, the SCC is met as long as $p(\Delta k = 0) < p(x_0 = \lambda_{e^-})$. This inequality implies that the SCC can be fulfilled in a phase-matched regime only if the pulse energy is higher than

$$E_{\text{min,SCC}}^{\text{HS}} = \frac{p_0 q_e \sqrt{2 Z_0} d^2}{16\pi^2 c^3 m_e k_B T K_1 K_2} \frac{I_{\text{peak}}^{3/2} \lambda_{\text{laser}}^5 N_{\text{cycles}}}{\Delta n \left(1 - \frac{\eta}{\eta_c}\right)}. \tag{6}$$

As shown in Supplement 1, it is possible to derive a more elaborate model accounting for the kinetic energy dependence of the electron mean free path. In this framework, the minimum pulse energy required not to infringe the SCC then reads

$$E_{\text{min,SCC}}^{\sigma} = \frac{p_0}{\pi c k_B T K_1 K_2} \frac{I_{\text{peak}} \lambda_{\text{laser}}^3 N_{\text{cycles}}}{\Delta n \left(1 - \frac{\eta}{\eta_c}\right)} \int_0^{x_0} g(x) \sigma(x) \mathrm{d}x, \tag{7}$$

where g is the radial distribution function of the atom [31], which describes how the atomic density varies in the vicinity of the atom.

The electron–neutral atom collision cross section, which is the sum of the elastic scattering, excitation, and ionization cross sections, is denoted σ [32,33].

It is *a priori* not possible to express the variables of the right hand sides of Eqs. (6) and (7) as a function of the other variables using a closed-form expression. However, as we show in Supplement 1, from the laser wavelength, one can determine the critical ionization level, the maximum cutoff energy that can be phase matched, its corresponding I_{peak}, and Δn [11] through an iterative algorithm. Then, the only remaining unknown is the ratio of the ionization level with the critical ionization level η/η_c. Using a previously published experimental result [6], we find $\eta/\eta_c = 91.8\%$ for HHG with a 620 eV cutoff in He. Inserting this value in Eq. (6) yields the minimum energy needed to obtain phase-matched harmonics while keeping $x_0 < \lambda_{e^-}$.

Figure 5(a) shows the results of this calculation in He for various driving wavelengths and number of cycles for the driving laser field. The corresponding cutoff energies and phase-matching pressures are shown in Fig. 5(b).

C. Availability of Laser Sources that Can Fulfill the SCC

We find that generating phase-matched harmonics throughout the complete water window (283–543 eV) while keeping the SCC valid requires, for example, a four-optical-cycle, 1.9 μm driver with a pulse energy of at least 0.4 mJ with the HS model, or at least 0.04 mJ with the $\sigma_{at/e^-}(E_{e^-})$ model. Similarly, with the HS model, we find that a four-optical-cycle, 2.8 μm driver with more than 2 mJ pulse energy is needed to generate keV harmonics within the SCC, while the $\sigma_{at/e^-}(E_{e^-})$ model predicts that more than 0.1 mJ are needed for this. Those values are at the limit or beyond of what the current laser technology allows for 100 kHz systems [5,6], but clearly within what has been achieved with state-of-the-art lasers operating at 10 kHz [58].

For longer wavelengths, tremendous developments in 2 μm pump lasers and parametric amplifiers have already enabled the generation of 0.75 mJ, 7 μm, eight-cycle pulses [41]. However, it is to be expected that pulses at the 1 to 10 mJ pulse energy level will be needed for an efficient generation of harmonics beyond 3–4 keV. Therefore, while it was shown theoretically and experimentally that the HHG efficiency is independent of pulse energy when absorption-limited HHG can be realized [8,67,68], our study shows that the HHG efficiency becomes dependent on the driving pulse energy when the SCC starts to be violated. This limit is particularly important for the generation of high photon energies. Furthermore, the minimum pulse energies required not to infringe the SCC found with the $\sigma_{at/e^-}(E_{e^-})$ model should be regarded as lower bounds. Indeed, as shown in Supplement 1, we assumed a probability of collision of 1 for the calculation of $E^{\sigma}_{min,\,SCC}$. However, we expect that even a lower probability of collision would already significantly impact the microscopic HHG yield.

As detailed in Supplement 1, calculations similar to those shown in Fig. 5 reveal that, compared to other gases, using He as the harmonics generation medium is optimum from the SCC point of view, since among all noble gases, it is the gas that requires the smallest laser pulse energy to generate a given SXR photon energy without infringing the SCC. Further, it is worth noting that another analysis part of Supplement 1 reveals that among elastic momentum transfer, atom excitation, and ionization, the latter process is the dominant mechanism responsible for the SCC breakdown in the SXR. This is because most collisions happen in the electron kinetic energy region between 0.1 and 1 keV, where the ionization cross section of all noble gases is higher than those of the other two processes.

D. Discussion of the Impact of the SCC Breakdown

We note that the values given in the previous paragraph are only estimates and should be regarded as orders of magnitude for pulse energies needed to prevent neighboring atoms from affecting the

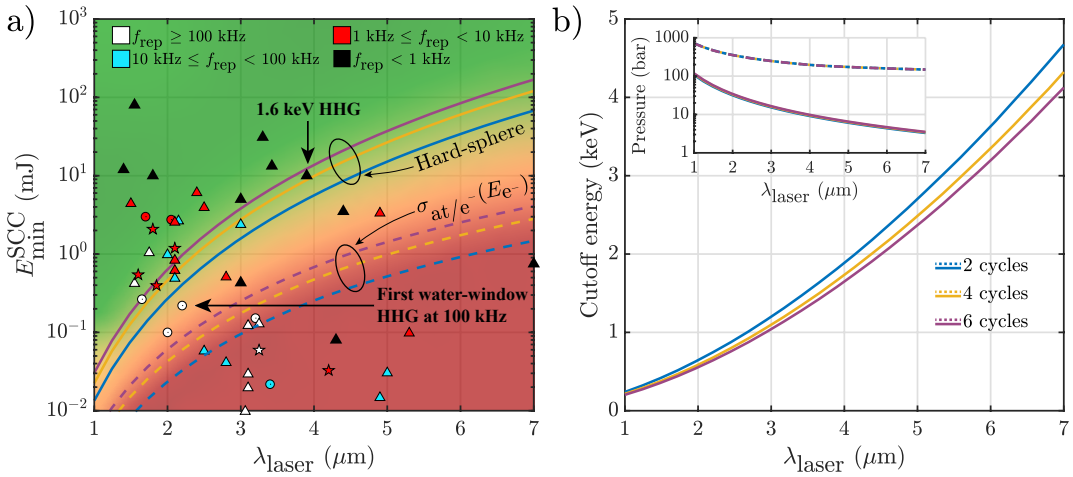

Fig. 5. Parameters required to phase match HHG in He keeping the SCC valid as a function of the driving wavelength using the hard-sphere- and kinetic-energy-dependent electron mean free path $\sigma_{at/e^-}(E_{e^-})$ models. (a) Minimum pulse energy needed to keep the SCC valid and phase match the HHG process (solid lines), and overview of laser systems delivering sub-two-cycle pulses (stars), $2 < N_{cycles} < 4$ (circles), and $4 > N_{cycles} > 20$ (triangles). Systems with a repetition rate lower than 1 kHz [34–43] are in black, those with 1 kHz $\leq f_{rep} <$ 10 kHz [44–57] are in red, those with 10 kHz $\leq f_{rep} <$ 100 kHz [58–61] are in blue, and those with $f_{rep} \geq$ 100 kHz [5,6,62–66] are in white. The background gradient represents the transition from the regime where the SCC is expected to be valid (green) to where it is infringed (red). For the kinetic-energy-dependent electron mean free path model $\sigma_{at/e^-}(E_{e^-})$, we use the parameters shown in Table 1 for the radial-distribution function. (b) Cutoff energies corresponding to the parameters shown in (a). The inset in (b) shows the phase-matching pressures corresponding to what is plotted in (a) and (b). Details about the calculation are in Supplement 1.

microscopic HHG response. Indeed, HHG up to 1.6 keV has already been demonstrated, with $x_0 \approx 3.5\lambda_{e^-}$ [3]. Despite the 35 bar pressure required for phase matching, the SXR flux was shown to still scale quadratically with pressure even at 1 keV, where $x_0 \approx 2\lambda_{e^-}$. This suggests that the microscopic HHG response was not greatly affected by surrounding atoms.

On the other hand, our previously published result [6] for phase-matched HHG in He up to 0.6 keV with $x_0 \approx 1.6\lambda_{e^-}$ showed that the SXR flux scaled as $\propto p^4$ instead of the usual $\propto p^2$ found in a typical phase-matched regime, indicating that the microscopic HHG response may have been affected by the high pressures used. As shown in Supplement 1, the difference between those two results may be due to the higher contribution of elastic momentum transfer at 2 μm compared to 3.9 μm, or to the different generation geometry: a waveguide was used for the 1.6 keV result, leading to an additional phase-matching term, while we used an unguided gas cell in our result.

To the best of our knowledge, those two results are the only ones where HHG was generated beyond the SCC breakdown. Further research is therefore required to determine the extent of the modification of the microscopic HHG response beyond the SCC breakdown, how phase matching may affect the coherent response depending on the generation geometry, how multiply scattered electrons are affected by surrounding atoms [69], and how each of the electron scattering processes affects the photoelectron wave packet and HHG efficiency. All those studies should soon become possible, due to the rapid progress in the development of high power OPCPAs pumped at 2 μm.

Finally, we stress that in a phase-matched regime, while the microscopic HHG response should be impacted by surrounding particles, incoherent emission is not expected to be significant. Indeed, phase matching HHG is usually achieved by keeping a low ionization level—typically below a percent in the SXR—leading to an incoherent emission level orders of magnitude lower than what we measured in the context of the high-intensity approach, where the ionization level is considerably higher than the critical ionization level.

5. CONCLUSION

We studied theoretically and experimentally the HHG regime where the photoelectron excursion in the continuum is of the order of the electron mean free path of the gas. For a typical 0.8 μm driver, we first found that this SCC breakdown occurs when intensities above $10^{16}-10^{17}\,\mathrm{W\cdot cm^{-2}}$ are used together with gas pressures around 10 bar. We then identified that producing phase-matched high harmonics with low pulse energies leads to a significant perturbation of the electron wave packet propagation by neighboring atoms. Indeed, phase matching SXR HHG requires high pressures, eventually leading to SCC breakdown. The main consequence of this is that a minimum pulse energy is required to stay in a regime where the SCC remains valid. This implies that mJ-level pulses are needed to generate phase-matched harmonics in the keV range without violating the SCC, even for few-cycle pulses. A second consequence is that, among all noble gases, using He as the generation medium is optimum from a SCC standpoint, as it is the noble gas that requires the lowest laser pulse energy to obtain a given HHG cutoff without infringing the SCC. A third consequence is that the shortest pulses possible should be used for the production of high harmonics, mostly because the phase-matching pressure is proportional to the number of optical cycles of the HHG driver. While further research is required to determine how the microscopic HHG response is affected by surrounding atoms when the SCC breaks down, we expect the HHG flux to decrease because of the modification of the photoelectron wave packet by surrounding particles. While so far very few experiments have been performed beyond this approximation, studies confirming the importance of SCC breakdown on the phase-matched HHG flux should become possible in the years to come, thanks to the fast development of long-wavelength lasers. Moreover, our findings may already explain the moderate conversion efficiencies of recently developed high-repetition-rate mid-infrared-driven HHG sources, and show that 1-to 10-mJ-level ultrashort laser sources will likely be needed for an efficient generation of multi-keV harmonics.

Funding. Schweizerischer Nationalfonds zur Förderung der Wissenschaftlichen Forschung (200020_200416); NCCR MUST (FAST initiative); National Science Foundation (2110633, theory of photoemission); Chemical Sciences, Geosciences, and Biosciences Division, Office of Basic Energy Sciences, Office of Science, U.S. Department of Energy (attosecond interferometry, DEFG02-86ER13491).

Acknowledgment. We acknowledge Götz Zinner for his valuable help in identifying the origin of the parasitic polarization. We also thank Yunpei Deng, Thomas Fennel, Anne L'Huillier, Cord Arnold, and Chen Guo for fruitful discussions.

Disclosures. The authors declare no conflicts of interest.

Data availability. Data underlying the results presented in this paper are available in an open research data repository [70], and the CTMC MATLAB code used for the simulations is available at [71].

Supplemental document. See Supplement 1 for supporting content.

REFERENCES

1. M. Lewenstein, P. Balcou, M. Y. Ivanov, A. L'Huillier, and P. B. Corkum, "Theory of high-harmonic generation by low-frequency laser fields," Phys. Rev. A **49**, 2117–2132 (1994).
2. P. B. Corkum, N. H. Burnett, and M. Y. Ivanov, "Subfemtosecond pulses," Opt. Lett. **19**, 1870–1872 (1994).
3. T. Popmintchev, M.-C. Chen, D. Popmintchev, P. Arpin, S. Brown, S. Alisauskas, G. Andriukaitis, T. Balciunas, O. D. Mucke, A. Pugzlys, A. Baltuska, B. Shim, S. E. Schrauth, A. Gaeta, C. Hernandez-Garcia, L. Plaja, A. Becker, A. Jaron-Becker, M. M. Murnane, and H. C. Kapteyn, "Bright coherent ultrahigh harmonics in the keV x-ray regime from mid-infrared femtosecond lasers," Science **336**, 1287–1291 (2012).
4. C. M. Heyl, C. L. Arnold, A. Couairon, and A. L'Huillier, "Introduction to macroscopic power scaling principles for high-order harmonic generation," J. Phys. B **50**, 013001 (2017).
5. M. Gebhardt, T. Heuermann, R. Klas, C. Liu, A. Kirsche, M. Lenski, Z. Wang, C. Gaida, J. E. Antonio-Lopez, A. Schülzgen, R. Amezcua-Correa, J. Rothhardt, and J. Limpert, "Bright, high-repetition-rate water window soft x-ray source enabled by nonlinear pulse self-compression in an antiresonant hollow-core fibre," Light Sci. Appl. **10**, 36 (2021).
6. J. Pupeikis, P.-A. Chevreuil, N. Bigler, L. Gallmann, C. R. Phillips, and U. Keller, "Water window soft x-ray source enabled by a 25 W few-cycle 2.2 μm OPCPA at 100 kHz," Optica **7**, 168–171 (2020).
7. V. V. Strelkov, V. T. Platonenko, and A. Becker, "High-harmonic generation in a dense medium," Phys. Rev. A **71**, 053808 (2005).
8. J. Rothhardt, M. Krebs, S. Hädrich, S. Demmler, J. Limpert, and A. Tünnermann, "Absorption-limited and phase-matched high harmonic generation in the tight focusing regime," New J. Phys. **16**, 033022 (2014).
9. C. B. Nakhosteen and K. Jousten, *Handbook of Vacuum Technology* (Wiley, 2016).
10. J. O. Hirschfelder, C. F. Curtiss, and R. B. Bird, *Molecular Theory of Gases and Liquids*, Structure of Matter Series (Wiley, 1964).

11. T. Popmintchev, M.-C. Chen, A. Bahabad, M. Gerrity, P. Sidorenko, O. Cohen, I. P. Christov, M. M. Murnane, and H. C. Kapteyn, "Phase matching of high harmonic generation in the soft and hard x-ray regions of the spectrum," Proc. Natl. Acad. Sci. USA **106**, 10516–10521 (2009).
12. J. L. Krause, K. J. Schafer, and K. C. Kulander, "High-order harmonic generation from atoms and ions in the high intensity regime," Phys. Rev. Lett. **68**, 3535–3538 (1992).
13. D. R. Miller, "Free jet sources," in *Atomic and Molecular Beam Methods*, G. Scoles, ed. (Oxford University, 1988), pp. 14–53.
14. V. P. Krainov, "Ionization rates and energy and angular distributions at the barrier-suppression ionization of complex atoms and atomic ions," J. Opt. Soc. Am. B **14**, 425–431 (1997).
15. P. M. Abanador, F. Mauger, K. Lopata, M. B. Gaarde, and K. J. Schafer, "Semiclassical modeling of high-order harmonic generation driven by an elliptically polarized laser field: the role of recolliding periodic orbits," J. Phys. B **50**, 035601 (2017).
16. A. N. Pfeiffer, C. Cirelli, M. Smolarski, D. Dimitrovski, M. Abu-samha, L. B. Madsen, and U. Keller, "Attoclock reveals natural coordinates of the laser-induced tunnelling current flow in atoms," Nat. Phys. **8**, 76–80 (2012).
17. P. Moreno, L. Plaja, and L. Roso, "High-order harmonic generation in a partially ionized medium," J. Opt. Soc. Am. B **13**, 430–435 (1996).
18. T. Ditmire, T. Donnelly, A. M. Rubenchik, R. W. Falcone, and M. D. Perry, "Interaction of intense laser pulses with atomic clusters," Phys. Rev. A **53**, 3379–3402 (1996).
19. S. Hrisafov, J. Pupeikis, P.-A. Chevreuil, F. Brunner, C. R. Phillips, L. Gallmann, and U. Keller, "High-power few-cycle near-infrared OPCPA for soft x-ray generation at 100 kHz," Opt. Express **28**, 40145–40154 (2020).
20. P.-A. Chevreuil, F. Brunner, S. Hrisafov, J. Pupeikis, C. R. Phillips, U. Keller, and L. Gallmann, "Water-window high harmonic generation with 0.8-μm and 2.2-μm OPCPAs at 100 kHz," Opt. Express **29**, 32996–33008 (2021).
21. G. Marcus, W. Helml, X. Gu, Y. Deng, R. Hartmann, T. Kobayashi, L. Strueder, R. Kienberger, and F. Krausz, "Subfemtosecond K-shell excitation with a few-cycle infrared laser field," Phys. Rev. Lett. **108**, 023201 (2012).
22. Y. Deng, Z. Zeng, Z. Jia, P. Komm, Y. Zheng, X. Ge, R. Li, and G. Marcus, "Ultrafast excitation of an inner-shell electron by laser-induced electron recollision," Phys. Rev. Lett. **116**, 073901 (2016).
23. Y. Deng, Z. Zeng, P. Komm, Y. Zheng, W. Helml, X. Xie, Z. Filus, M. Dumergue, R. Flender, M. Kurucz, L. Haizer, B. Kiss, S. Kahaly, R. Li, and G. Marcus, "Laser-induced inner-shell excitations through direct electron re-collision versus indirect collision," Opt. Express **28**, 23251–23265 (2020).
24. J. Seres, P. Wobrauschek, C. Streli, V. S. Yakovlev, E. Seres, F. Krausz, and C. Spielmann, "Generation of coherent keV x-rays with intense femtosecond laser pulses," New J. Phys. **8**, 251–254 (2006).
25. J. Gao, J. Gao, J. Wu, J. Wu, Z. Lou, F. Yang, F. Yang, J. Qian, J. Qian, Y. Peng, Y. Peng, Y. Leng, Y. Leng, Y. Zheng, Y. Zheng, Y. Zheng, Z. Zeng, Z. Zeng, Z. Zeng, R. Li, and R. Li, "High-order harmonic generation in an x-ray range from laser-induced multivalent ions of noble gas," Optica **9**, 1003–1008 (2022).
26. E. Seres, J. Seres, F. Krausz, and C. Spielmann, "Generation of coherent soft-x-ray radiation extending far beyond the titanium L edge," Phys. Rev. Lett. **92**, 163002 (2004).
27. M. Geissler, G. Tempea, and T. Brabec, "Phase-matched high-order harmonic generation in the nonadiabatic limit," Phys. Rev. A **62**, 033817 (2000).
28. G. Tempea, M. Geissler, M. Schnürer, and T. Brabec, "Self-phase-matched high harmonic generation," Phys. Rev. Lett. **84**, 4329–4332 (2000).
29. C. Vozzi, M. Negro, F. Calegari, S. Stagira, K. Kovács, and V. Tosa, "Phase-matching effects in the generation of high-energy photons by mid-infrared few-cycle laser pulses," New J. Phys. **13**, 073003 (2011).
30. S. Demmler, J. Rothhardt, S. Hädrich, M. Krebs, A. Hage, J. Limpert, and A. Tünnermann, "Generation of high photon flux coherent soft x-ray radiation with few-cycle pulses," Opt. Lett. **38**, 5051–5054 (2013).
31. D. Chandler and J. K. Percus, "Introduction to modern statistical mechanics," Phys. Today **41**(12), 114–118 (1988).
32. E. Carbone, W. Graef, G. Hagelaar, D. Boer, M. M. Hopkins, J. C. Stephens, B. T. Yee, S. Pancheshnyi, J. van Dijk, and L. Pitchford, "Data needs for modeling low-temperature non-equilibrium plasmas: the LXCat project, history, perspectives and a tutorial," Atoms **9**, 16 (2021).
33. R. I. Golyatina and S. A. Maiorov, "Analytical approximation of cross sections of collisions of electrons with inert gas atoms," Plasma Phys. Rep. **48**, 193–199 (2022).
34. E. J. Takahashi, T. Kanai, K. L. Ishikawa, Y. Nabekawa, and K. Midorikawa, "Coherent water window x ray by phase-matched high-order harmonic generation in neutral media," Phys. Rev. Lett. **101**, 253901 (2008).
35. G. Andriukaitis, T. Balčiūnas, S. Ališauskas, A. Pugžlys, A. Baltuška, T. Popmintchev, M.-C. Chen, M. M. Murnane, and H. C. Kapteyn, "90 GW peak power few-cycle mid-infrared pulses from an optical parametric amplifier," Opt. Lett. **36**, 2755–2757 (2011).
36. K. Zhao, H. Zhong, P. Yuan, G. Xie, J. Wang, J. Ma, and L. Qian, "Generation of 120 GW mid-infrared pulses from a widely tunable noncollinear optical parametric amplifier," Opt. Lett. **38**, 2159–2161 (2013).
37. N. Thiré, S. Beaulieu, V. Cardin, A. Laramée, V. Wanie, B. E. Schmidt, and F. Légaré, "10 mJ 5-cycle pulses at 1.8 μm through optical parametric amplification," Appl. Phys. Lett. **106**, 091110 (2015).
38. Y. Fu, K. Nishimura, R. Shao, A. Suda, K. Midorikawa, P. Lan, and E. J. Takahashi, "High efficiency ultrafast water-window harmonic generation for single-shot soft X-ray spectroscopy," Commun. Phys. **3**, 92 (2020).
39. J. Alves, H. Pires, C. P. Joáo, and G. Figueira, "Multi-mJ scaling of 5-optical cycle, 3 μm OPCPA," Photonics **8**, 503 (2021).
40. Y. Fu, B. Xue, K. Midorikawa, and E. J. Takahashi, "TW-scale mid-infrared pulses near 3.3 μm directly generated by dual-chirped optical parametric amplification," Appl. Phys. Lett. **112**, 241105 (2018).
41. U. Elu, T. Steinle, D. Sánchez, L. Maidment, K. Zawilski, P. Schunemann, U. D. Zeitner, C. Simon-Boisson, and J. Biegert, "Table-top high-energy 7 μm OPCPA and 260 mJ Ho:YLF pump laser," Opt. Lett. **44**, 3194–3197 (2019).
42. E. Migal, A. Pushkin, B. Bravy, V. Gordienko, N. Minaev, A. Sirotkin, and F. Potemkin, "3.5-mJ 150-fs Fe:ZnSe hybrid mid-IR femtosecond laser at 4.4 μm for driving extreme nonlinear optics," Opt. Lett. **44**, 2550–2553 (2019).
43. M. Bridger, O. A. Naranjo-Montoya, A. Tarasevitch, and U. Bovensiepen, "Towards high power broad-band OPCPA at 3000 nm," Opt. Express **27**, 31330–31337 (2019).
44. S. L. Cousin, N. Di Palo, B. Buades, S. M. Teichmann, M. Reduzzi, M. Devetta, A. Kheifets, G. Sansone, and J. Biegert, "Attosecond streaking in the water window: a new regime of attosecond pulse characterization," Phys. Rev. X **7**, 041030 (2017).
45. V. E. Leshchenko, B. K. Talbert, Y. H. Lai, S. Li, Y. Tang, S. J. Hageman, G. Smith, P. Agostini, L. F. DiMauro, and C. I. Blaga, "High-power few-cycle Cr:ZnSe mid-infrared source for attosecond soft x-ray physics," Optica **7**, 981–988 (2020).
46. D. Popmintchev, B. R. Galloway, M.-C. Chen, F. Dollar, C. A. Mancuso, A. Hankla, L. Miaja-Avila, G. O'Neil, J. M. Shaw, G. Fan, S. Ališauskas, G. Andriukaitis, T. Balčiunas, O. D. Mücke, A. Pugzlys, A. Baltuška, H. C. Kapteyn, T. Popmintchev, and M. M. Murnane, "Near- and extended-edge x-ray-absorption fine-structure spectroscopy using ultrafast coherent high-order harmonic supercontinua," Phys. Rev. Lett. **120**, 093002 (2018).
47. N. Ishii, K. Kaneshima, K. Kitano, T. Kanai, S. Watanabe, and J. Itatani, "Carrier-envelope phase-dependent high harmonic generation in the water window using few-cycle infrared pulses," Nat. Commun. **5**, 3331 (2014).
48. K.-H. Hong, S.-W. Huang, J. Moses, X. Fu, C.-J. Lai, G. Cirmi, A. Sell, E. Granados, P. Keathley, and F. X. Kärtner, "High-energy, phase-stable, ultrabroadband kHz OPCPA at 2.1 μm pumped by a picosecond cryogenic Yb:YAG laser," Opt. Express **19**, 15538–15548 (2011).
49. F. Silva, P. K. Bates, A. Esteban-Martin, M. Ebrahim-Zadeh, and J. Biegert, "High-average-power, carrier-envelope phase-stable, few-cycle pulses at 2.1 μm from a collinear BiB3O6 optical parametric amplifier," Opt. Lett. **37**, 933–935 (2012).
50. Y. Deng, A. Schwarz, H. Fattahi, M. Ueffing, X. Gu, M. Ossiander, T. Metzger, V. Pervak, H. Ishizuki, T. Taira, T. Kobayashi, G. Marcus, F. Krausz, R. Kienberger, and N. Karpowicz, "Carrier-envelope-phase-stable, 1.2 mJ, 1.5 cycle laser pulses at 2.1 μm," Opt. Lett. **37**, 4973–4975 (2012).
51. C. Schmidt, Y. Pertot, T. Balciunas, K. Zinchenko, M. Matthews, H. J. Wörner, and J.-P. Wolf, "High-order harmonic source spanning up to

the oxygen K-edge based on filamentation pulse compression," Opt. Express **26**, 11834–11842 (2018).
52. H. He, Z. Wang, C. Hu, J. Jiang, S. Qin, P. He, N. Zhang, P. Yang, Z. Li, and Z. Wei, "520-μJ mid-infrared femtosecond laser at 2.8 μm by 1-kHz KTA optical parametric amplifier," Appl. Phys. B **124**, 31 (2018).
53. L. von Grafenstein, M. Bock, D. Ueberschaer, E. Escoto, A. Koç, K. Zawilski, P. Schunemann, U. Griebner, and T. Elsaesser, "Multi-millijoule, few-cycle 5 μm OPCPA at 1 kHz repetition rate," Opt. Lett. **45**, 5998–6001 (2020).
54. P. Malevich, T. Kanai, H. Hoogland, R. Holzwarth, A. Baltuška, and A. Pugžlys, "Broadband mid-infrared pulses from potassium titanyl arsenate/zinc germanium phosphate optical parametric amplifier pumped by Tm, Ho-fiber-seeded Ho:YAG chirped-pulse amplifier," Opt. Lett. **41**, 930–933 (2016).
55. Y. Wu, F. Zhou, E. W. Larsen, F. Zhuang, Y. Yin, and Z. Chang, "Generation of few-cycle multi-millijoule 2.5 μm pulses from a single-stage Cr2+:ZnSe amplifier," Sci. Rep. **10**, 7775 (2020).
56. Y. Yin, J. Li, X. Ren, K. Zhao, Y. Wu, E. Cunningham, and Z. Chang, "High-efficiency optical parametric chirped-pulse amplifier in BiB3O6 for generation of 3 mJ, two-cycle, carrier-envelope-phase-stable pulses at 1.7 μm," Opt. Lett. **41**, 1142–1145 (2016).
57. C.-J. Lai, K.-H. Hong, J. P. Siqueira, P. Krogen, C.-L. Chang, G. J. Stein, H. Liang, P. D. Keathley, G. Laurent, J. Moses, L. E. Zapata, and F. X. Kärtner, "Multi-mJ mid-infrared kHz OPCPA and Yb-doped pump lasers for tabletop coherent soft x-ray generation," J. Opt. **17**, 094009 (2015).
58. T. Feng, A. Heilmann, M. Bock, L. Ehrentraut, T. Witting, H. Yu, H. Stiel, S. Eisebitt, and M. Schnürer, "27 W 2.1 μm OPCPA system for coherent softx-ray generation operating at 10 kHz," Opt. Express **28**, 8724–8733 (2020).
59. X. Zou, W. Li, S. Qu, K. Liu, H. Li, Q. J. Wang, Y. Zhang, and H. Liang, "Flat-top pumped multi-millijoule mid-infrared parametric chirped-pulse amplifier at 10 kHz repetition rate," Laser Photon. Rev. **15**, 2000292 (2021).
60. J. H. Buss, I. Grguras, S. Starosielec, M. V. Petev, T. Golz, M. Schulz, M. J. Prandolini, P. Kraus, F. Campi, and R. Riedel, "High-power OPCPAs at 1450–2400 nm wavelength," Proc. SPIE **11670**, 116700Y (2021).
61. J. H. Buss, S. Starosielec, I. Grguras, T. Golz, M. Prandolini, M. Schulz, P. Kraus, and R. Riedel, "Few-cycle OPCPA at 2 μm with up to 100 W average power," in *OSA High-brightness Sources and Light-driven Interactions Congress 2020 (EUVXRAY, HILAS, MICS)* (OSA, 2020), paper HF1B.3.
62. M. Neuhaus, H. Fuest, M. Seeger, J. Schötz, M. Trubetskov, P. Russbueldt, H. D. Hoffmann, E. Riedle, Z. Major, V. Pervak, M. F. Kling, and P. Wnuk, "10 W CEP-stable few-cycle source at 2 μm with 100 kHz repetition rate," Opt. Express **26**, 16074–16085 (2018).
63. N. Thiré, R. Maksimenka, B. Kiss, C. Ferchaud, G. Gitzinger, T. Pinoteau, H. Jousselin, S. Jarosch, P. Bizouard, V. Di Pietro, E. Cormier, K. Osvay, and N. Forget, "Highly stable, 15 W, few-cycle, 65 mrad CEP-noise mid-IR OPCPA for statistical physics," Opt. Express **26**, 26907–26915 (2018).
64. U. Elu, M. Baudisch, H. Pires, F. Tani, M. H. Frosz, F. Köttig, A. Ermolov, P. St.J. Russell, and J. Biegert, "High average power and single-cycle pulses from a mid-IR optical parametric chirped pulse amplifier," Optica **4**, 1024–1029 (2017).
65. M. Mero, Z. Heiner, V. Petrov, H. Rottke, F. Branchi, G. M. Thomas, and M. J. J. Vrakking, "43 W, 1.55 μm and 12.5 W, 3.1 μm dual-beam, sub-10 cycle, 100 kHz optical parametric chirped pulse amplifier," Opt. Lett. **43**, 5246–5249 (2018).
66. M. K. R. Windeler, K. Mecseki, A. Miahnahri, J. S. Robinson, J. M. Fraser, A. R. Fry, and F. Tavella, "100 W high-repetition-rate near-infrared optical parametric chirped pulse amplifier," Opt. Lett. **44**, 4287–4290 (2019).
67. C. M. Heyl, H. Coudert-Alteirac, M. Miranda, M. Louisy, K. Kovacs, V. Tosa, E. Balogh, K. Varjú, A. L'Huillier, A. Couairon, and C. L. Arnold, "Scale-invariant nonlinear optics in gases," Optica **3**, 75–81 (2016).
68. T. Brabec and F. Krausz, "Intense few-cycle laser fields: frontiers of nonlinear optics," Rev. Mod. Phys. **72**, 545–591 (2000).
69. J. Seres, E. Seres, B. Landgraf, B. Ecker, B. Aurand, T. Kuehl, and C. Spielmann, "High-harmonic generation and parametric amplification in the soft x-rays from extended electron trajectories," Sci. Rep. **4**, 4234 (2014).
70. P. A. Chevreuil, F. Brunner, U. Thumm, U. Keller, and L. Gallmann, "Breakdown of the single-collision condition for soft x-ray high harmonic generation in noble gases: dataset," ETH Zurich Research Collection (2022) https://doi.org/10.3929/ethz-b-000581229.
71. P. A. Chevreuil, "Codes to compute individual electron trajectories in the Barrier-Suppression Ionisation regime," Github (2022) https://github.com/pierre-alexis-chevreuil/BSI-CTMC.